AIChE WILEY InterScience® DISCOVER SOMETHING GREAT

PARTICLE TECHNOLOGY AND FLUIDIZATION

Filtered Two-Fluid Models for Fluidized Gas-Particle Suspensions

Yesim Igci, Arthur T. Andrews IV, and Sankaran Sundaresan
Dept. of Chemical Engineering, Princeton University, Princeton, NJ 08544

Sreekanth Pannala
Oak Ridge National Laboratory, Oak Ridge, TN 37831

Thomas O'Brien
National Energy Technology Laboratory, Morgantown, WV 26507

DOI 10.1002/aic.11481
Published online March 28, 2008 in Wiley InterScience (www.interscience.wiley.com).

Starting from a kinetic theory based two-fluid model for gas-particle flows, we first construct filtered two-fluid model equations that average over small scale inhomogeneities that we do not wish to resolve in numerical simulations. We then outline a procedure to extract constitutive models for these filtered two-fluid models through highly resolved simulations of the kinetic theory based model equations in periodic domains. Two- and three-dimensional simulations show that the closure relations for the filtered two-fluid models manifest a definite and systematic dependence on the filter size. Linear stability analysis of the filtered two-fluid model equations reveals that filtering does indeed remove small scale structures that are afforded by the microscopic two-fluid model. © 2008 American Institute of Chemical Engineers *AIChE J,* 54: 1431–1448, 2008
Keywords: circulating fluidized beds, computational fluid dynamics (CFD), fluidization, particle technology, fluid mechanics

Introduction

Chemical reactors that take the form of fluidized beds and circulating fluidized beds are widely used in energy-related and chemical process industries.[1] Gas-particle flows in these devices are inherently unstable; they manifest fluctuations over a wide range of length and time scales. Analysis of the performance of large scale fluidized bed processes through computational simulations of hydrodynamics and energy/species transport is becoming increasingly common. In the present study, we are concerned with the development of hydrodynamic models that are useful for simulation of gas-particle flows in large scale fluidized processes.

Correspondence concerning this article should be addressed to S. Sundaresan at sundar@princeton.edu.

The number of particles present in most gas-particle flow systems is large, rendering detailed description of the motion of all the particles and fluid elements impractical. Hence, two-fluid model equations[2–4] are commonly employed to probe the flow characteristics, and species and energy transport. In this approach, the gas and particle phases are treated as interpenetrating continua, and locally averaged quantities such as the volume fractions, velocities, species concentrations, and temperatures of gas and particle phases appear as dependent field variables. The averaging process leading to two-fluid model equations erases the details of flow at the level of individual particles; but their consequences appear in the averaged equations through terms for which one must develop constitutive relations. For example, in the momentum balance equations, constitutive relations are needed for the gas-particle interaction force and the effective stresses in the gas and particle phases.

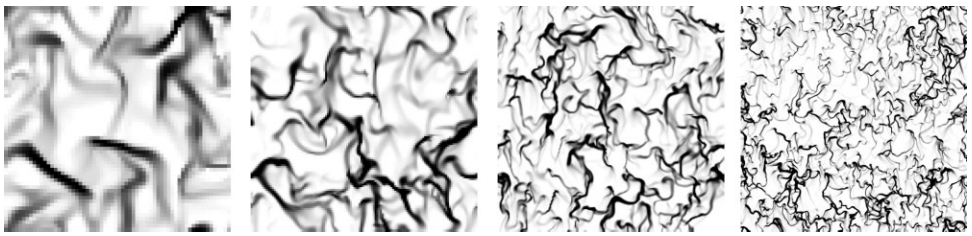

Figure 1. Snapshots of the particle volume fraction field in a large periodic domain of size 131.584 × 131.584 dimensionless units are displayed.

The physical conditions corresponding to these simulations are listed in Table 2. The domain-average particle volume fraction, $\langle \phi_s \rangle = 0.05$ Simulations were performed with different resolutions: (a) 64 × 64 grids; (b) 128 × 128 grids; (c) 256 × 256 grids; (d) 512 × 512 grids. The gray scale axis ranges from $\phi_s = 0.00$ (white) to $\phi_s = 0.25$ (black).

The general form of the two-fluid model equations is fairly standard and this has permitted the development of numerical algorithms for solving them. For example, open-source packages such as MFIX[4,5] and commercial software (e.g., Fluent®) can readily be applied to perform transient integration (of the discretized forms) of the balance equations governing reactive and non-reactive multiphase flows. The results generated through such simulations are dependent on the postulated constitutive models, and a major focus of research over the past few decades has been on the improvement of these constitutive models.

Through a combination of experiments and computer simulations, constitutive relations have been developed in the literature for the fluid–particle interaction force and the effective stresses in the fluid and particle phases. In gas-particle systems, the interaction force is predominantly due to the drag force. An empirical drag law that bridges the results of Wen and Yu[6] for dilute systems and the Ergun[7] approach for dense systems is widely used in simulation studies.[2] In the past decade, ab initio drag force models have also been developed via detailed simulations of fluid flow around assemblies of particles.[8–14]

The Stokes number associated with the particles in many gas-particle mixtures is sufficiently large that particle–particle and particle–wall collisions do occur; furthermore, when the particle volume fraction is below ~0.5, the particle–particle interactions occur largely through binary collisions. The particle phase stress in these systems is widely modeled through the kinetic theory of granular materials.[2,15,16] This kinetic theory approach has also been extended to systems containing mixtures of different types of particles.[2,17–20]

It is important to keep in mind that all these closures are derived from data or analysis of nearly homogeneous systems. Henceforth, we will refer to the two-fluid model equations coupled with constitutive relations deduced from nearly homogeneous systems as the microscopic two-fluid model equations. For example, the kinetic theory based model equations described and simulated in most of the literature references fall in this category.[2,16–31]

A practical difficulty comes about when one tries to solve these microscopic two-fluid model equations for gas-particle flows. Gas-particle flows in fluidized beds and riser reactors are inherently unstable, and they manifest inhomogeneous structures over a wide range of length and time scales. There is a substantial body of literature, where researchers have sought to capture these fluctuations through numerical simulation of microscopic two-fluid model equations. Indeed, two-fluid models for such flows reveal unstable modes whose length scale is as small as 10 particle diameters.[30,31] This can readily be ascertained by simple simulations, as illustrated in Figure 1. Transient simulations of a fluidized suspension of ambient air and typical Fluid Catalytic Cracking catalyst particles were performed (using MFIX[4,5]) in a Cartesian, two-dimensional (2D), periodic domain at different grid resolutions; these simulations employed kinetic theory-based (microscopic) two-fluid model equations (summarized in Table 1 and briefly discussed in the *Microscopic Two-fluid Model Equations* section below). The relevant parameter values can be found in Table 2. The simulations revealed that an initially homogeneous suspension gave way to an inhomogeneous state with persistent fluctuations. Snapshots of the particle volume fraction fields obtained in simulations with different spatial grid resolution are shown in Figure 1. It is readily apparent that finer and finer structures are resolved as the spatial grid is refined. Statistical quantities obtained by averaging over the whole domain were found to depend on the grid resolution employed in the simulations and they became nearly grid-size independent only when grid sizes of the order of 10 particle diameters were used (see Agrawal et al.[30] for further discussion). Thus, if one sets out to solve the microscopic two-fluid model equations for gas-particle flows, grid sizes of the order of 10 particle diameters become necessary. Moreover, such fine spatial resolution reduces the time steps required, further increasing the computational effort. For most devices of practical (commercial) interest, such extremely fine spatial grids and small time steps are unaffordable.[32] Indeed, gas-particle flows in large fluidized beds and risers are often simulated by solving discretized versions of the two-fluid model equations over a coarse spatial grid. Such coarse grid simulations do not resolve the small-scale (i.e., subgrid scale) spatial structures which, according to the microscopic two-fluid equations and experimental observation, do indeed exist. The effect of these unresolved structures on the structures resolved in coarse-grid simulations must be accounted for through appropriate modifications to the closures—for example, the effective drag coefficient in the coarse-grid simulations will be smaller than that in the microscopic two-fluid model to reflect the tendency of the gas to flow more easily around the unresolved clusters[30,31] than through a homogenous distribution of these

Table 1. Model Equations for Gas-Particle Flows

$$\frac{\partial \rho_s \phi_s}{\partial t} + \nabla \cdot (\rho_s \phi_s \mathbf{v}) = 0 \tag{1}$$

$$\frac{\partial (\rho_g (1-\phi_s))}{\partial t} + \nabla \cdot \left[\rho_g (1-\phi_s)\mathbf{u}\right] = 0 \tag{2}$$

$$\left[\frac{\partial (\rho_g \phi_s \mathbf{v})}{\partial t} + \nabla \cdot (\rho_g \phi_s \mathbf{v}\mathbf{v})\right] = -\nabla \cdot \boldsymbol{\sigma}_s - \phi_s \nabla \cdot \boldsymbol{\sigma}_g + \mathbf{f} + \rho_s \phi_s \mathbf{g} \tag{3}$$

$$\left[\frac{\partial (\rho_g (1-\phi_s)\mathbf{u})}{\partial t} + \nabla \cdot \left(\rho_g (1-\phi_s)\mathbf{u}\mathbf{u}\right)\right] = -(1-\phi_s)\nabla \cdot \boldsymbol{\sigma}_g - \mathbf{f} + \rho_g (1-\phi_s)\mathbf{g} \tag{4}$$

$$\left[\frac{\partial \left(\frac{3}{2}\rho_s \phi_s \mathrm{T}\right)}{\partial t} + \nabla \cdot \left(\frac{3}{2}\rho_s \phi_s \mathrm{T}\mathbf{v}\right)\right] = -\nabla \cdot \mathbf{q} - \boldsymbol{\sigma}_s : \nabla \mathbf{v} + \Gamma_{slip} - \mathrm{J}_{coll} - \mathrm{J}_{vis} \tag{5}$$

Gas phase stress tensor

$$\boldsymbol{\sigma}_g = p_g \mathbf{I} - \hat{\mu}_g \left[\nabla \mathbf{u} + (\nabla \mathbf{u})^{\mathrm{T}} - \frac{2}{3}(\nabla \cdot \mathbf{u})\mathbf{I}\right] \tag{6}$$

Gas-particle drag (Wen and Yu[6])

$$\mathbf{f} = \beta(\mathbf{u} - \mathrm{v}); \beta = \frac{3}{4} C_D \frac{\rho_g (1-\phi_s)\phi_s |\mathbf{u} - \mathrm{v}|}{d} (1-\phi_s)^{-2.65} \tag{7}$$

$$\mathrm{C_D} = \begin{cases} \dfrac{24}{Re_g}(1 + 0.15\mathrm{Re_g}^{0.687}) & Re_g < 1000 \\ 0.44 & Re_g \geq 1000 \end{cases}; \; Re_g = \frac{(1-\phi_s)\rho_g d|\mathbf{u} - \mathbf{v}|}{\mu_g}$$

Kinetic theory model for particle phase stress

$$\boldsymbol{\sigma}_s = [p_s - \eta \mu_b (\nabla \cdot \mathbf{v})]\mathbf{I} - 2\mu_s \mathbf{S} \tag{8}$$

where $p_s = \rho_s \phi_s (1 + 4\eta \phi_s g_o)\mathrm{T}, \mathbf{S} = \frac{1}{2}\left(\nabla \mathbf{v} + (\nabla \mathbf{v})^{\mathrm{T}}\right) - \frac{1}{3}(\nabla \cdot \mathbf{v})\mathbf{I}$

$$\mu_s = \left(\frac{2+\alpha}{3}\right)\left\{\frac{\mu^*}{g_o \eta (2-\eta)}\left(1 + \frac{8}{5}\phi_s \eta g_o\right)\left(1 + \frac{8}{5}\eta(3\eta - 2)\phi_s g_o\right) = \frac{3}{5}\eta \mu_b\right\}$$

$$\mu^* = \frac{\mu}{1 + \frac{2\beta\mu}{(\rho_s \phi_s)^2 g_0 \mathrm{T}}}; \; \mu = \frac{5\rho_s d\sqrt{\pi \mathrm{T}}}{96};$$

$$\mu_b = \frac{256\mu\phi_s^2 g_o}{5\pi}; \; \eta = \frac{(1+e_p)}{2}; \; g_o = \frac{1}{1 - (\phi_s/\phi_{s,max})^{1/3}}; \; \phi_{s,max} = 0.65; \alpha = 1.6$$

Kinetic theory model for pseudo-thermal energy flux

$$\mathbf{q} = -\lambda_s \nabla \mathrm{T} \tag{9}$$

where $\lambda_s = \frac{\lambda^*}{g_o}\left\{\left(1 + \frac{12}{5}\eta\phi_s g_o\right)\left(1 + \frac{12}{5}\eta^2(4\eta - 3)\phi_s g_o\right) + \frac{64}{25\pi}(41 - 33\eta)\eta^2 \phi_s^2 g_o^2\right\}$

$$\lambda^* = \frac{\lambda}{1 + \frac{6\beta\lambda}{5(\rho_s \phi_s)^2 g_o \mathrm{T}}}; \; \lambda = \frac{75\rho_s d\sqrt{\pi \mathrm{T}}}{48\eta(41 - 33\eta)}$$

Table 1. (Continued)

Kinetic theory model for rate of dissipation of pseudo-thermal energy through collisions

$$J_{coll} = \frac{48}{\sqrt{\pi}}\eta(1-\eta)\frac{\rho_s \phi_s^2}{d} g_o T^{3/2} \tag{10}$$

Effect of fluid on particle phase fluctuation energy (Koch and Sangani[16])

$$J_{vis} = \frac{54\phi_s \mu_g T}{d^2} R_{diss}, \quad \text{where}$$

$$R_{diss} = 1 + \frac{3\phi_s^{1/2}}{\sqrt{2}} + \frac{135}{64}\phi_s \ln \phi_s + 11.26\phi_s(1 - 5.1\phi_s + 16.57\phi_s^2 - 21.77\phi_s^3) - \phi_s \mathbf{g_o} \ln(0.01) \tag{11}$$

$$\Gamma_{slip} = \frac{81\phi_s \mu_g^2 |\mathbf{u} - \mathbf{v}|}{g_o d^3 \rho_g \sqrt{\pi T}} \Psi, \quad \text{where} \tag{12}$$

$$\Psi = \frac{R_d^2}{(1 + 3.5\phi_s^{1/2} + 5.9\phi_s)},$$

$$R_d = \begin{cases} \dfrac{1 + 3(\phi_s/2)^{1/2} + (135/64)\phi_s \ln\phi_s + 17.14\phi_s}{1 + 0.681\phi_s - 8.48\phi_s^2 + 8.16\phi_s^3}, \phi_s < 0.4 \\ \dfrac{10\phi_s}{(1-\phi_s)^3} + 0.7, \phi_s \geq 0.4 \end{cases}$$

particles. Qualitatively, this is equivalent to an effectively larger apparent size for the particles.

One can readily pursue this line of thought and examine the influence of these unresolved structures on the effective interphase transfer and dispersion coefficients which should be used in coarse-grid simulations. Inhomogeneous distribution of particles will promote bypassing of the gas around the particle-rich regions and this will necessarily decrease the effective interphase mass and energy transfer rates. Conversely, fluctuations associated with the small scale inhomogeneities will contribute to the dispersion of the particles and the gas, but this effect will be unaccounted for in the coarse-grid simulations of the microscopic two-fluid models.

Researchers have approached this problem of treating unresolved structures through various approximate schemes. O'Brien and Syamlal,[33] Boemer et al.[34] and Heynderickx et al.[35] pointed out the need to correct the drag coefficient to account for the consequence of clustering, and proposed a correction for the very dilute limit. Some authors have used an apparent cluster size in an effective drag coefficient closure as a tuning parameter,[36] others have deduced corrections to the drag coefficient using an energy minimization multiscale approach.[37] The concept of particle phase turbulence has also been explored to introduce the effect of the fluctuations associated with clusters and streamers on the particle phase stresses.[38,39] However, a systematic approach that combines the influence of the unresolved structures on the drag coefficient and the stresses has not yet emerged. The effects of these unresolved structures on interphase transfer and dispersion coefficients remain unexplored.

Agrawal et al.[30] showed that the effective drag law and the effective stresses, obtained by averaging (the results gathered in highly resolved simulations of a set of microscopic two-fluid model equations) over the whole (periodic) domain, were very different from those used in the microscopic two-fluid model and that they depended on size of the periodic domain. They also demonstrated that all the effects seen in the 2D simulations persisted when simulations were repeated in three dimensions (3D) and that both 2D and 3D simulations revealed the same qualitative trends. Andrews et al.[31] performed many highly resolved simulations of fluidized gas-particle mixtures in a 2D periodic domain, whose total size coincided with that of the grid size in an anticipated large-scale riser flow simulation. Using these numerical results, they constructed ad hoc subgrid models for the effects of the fine-scale flow structures on the drag force and the stresses, and examined the consequence of these subgrid models on the outcome of the coarse-grid simulations of gas-particle flow in a large-scale vertical riser. They demonstrated that these subgrid scale corrections affect the predicted large-scale flow patterns profoundly.[31]

Thus, it is clear that one must carefully examine whether a microscopic two-fluid model must be modified to introduce

Table 2. Physical Properties of Gas and Solids

d	Particle diameter	7.5×10^{-6} m
ρ_s	Particle density	1500 kg/m^3
ρ_g	Gas density	1.3 kg/m^3
μ_g	Gas viscosity	1.8×10^{-5} kg/m s
e_p	Coefficient of restitution	0.9
v_t	Terminal settling velocity	0.2184 m/s
v_t^2/g	Characteristic length	0.00487 m
v_t/g	Characteristic time	0.0223 s
$\rho_s v_t^2$	Characteristic stress	71.55 kg/m s^2

the effects of unresolved structures before embarking on coarse-grid simulations of gas-particle flows. In the study by Andrews et al.,[31] the filtering was done simply by choosing the filter size to be the grid size in the coarse-grid simulation of the filtered equations. Furthermore, the corrections accounting for the effects of the structures that would not be resolved in the coarse-grid simulations were extracted from highly resolved simulations performed in a periodic domain whose size was chosen to be the same as the filter size; this imposed periodicity necessarily limited the dynamics of the structures in the highly resolved simulations and so the accuracy of using the subgrid models deduced from such restrictive simulations is debatable.

The first objective of the present study is to develop a systematic filtering approach and construct closure relationships for the drag coefficient and the effective stresses in the gas and particle phases that are appropriate for coarse-grid simulations of gas-particle flows. Briefly, we have performed highly resolved simulations of a kinetic theory based two-fluid model in a large periodic domain, and analyzed the results using different filter sizes. In this case, as the filter size is considerably smaller than the periodic domain size, the microstructures sampled in the filtered region are not constrained by the periodic boundary conditions. The present approach also exposes nicely the filter size dependence of various quantities.

It should be emphasized that the present study neither challenges the validity of the microscopic two-fluid model equations such as the kinetic theory based equations nor assumes that they are exactly correct. Instead, it uses these microscopic equations as a starting point and seeks modifications to make them suitable for coarse-grid simulations. (If a fine grid can be used to resolve all the structures contained in the microscopic two-fluid model equations, the present analysis is unnecessary; however, such high resolution is neither practical nor desirable for the analysis of the macroscale flow behavior.) As more accurate microscopic two-fluid models emerge, one can readily use such models to refine the results presented here.

The second objective of the present study is to demonstrate that filtering does indeed remove small scale structures that are afforded by the microscopic two-fluid models. If filtering has been done in a meaningful manner, the filtered equations should yield coarser structures than the microscopic two-fluid model (from which the filtered equations were derived). We will demonstrate that this is indeed the case through one-dimensional linear stability analysis of the filtered model equations.

Microscopic Two-Fluid Model Equations

The general form of the two-fluid model equations for gas-particle flows is fairly standard. However, several choices have been discussed and analyzed in the literature for the constitutive relations for the fluid-particle drag force and the effective stresses.[2,3,12] We consider a system consisting of uniformly sized particles and focus on the situation, where the particles interact only through binary collisions. In the kinetic theory approach, the continuity and momentum equations for the gas and particle phases are supplemented by an equation describing the evolution of the fluctuation energy (a.k.a. granular energy) associated with the particles, which is used to compute the local granular temperature; the particle phase stress is then expressed in terms of the local particle volume fraction, granular temperature, rate of deformation, and particle properties. There are several different closures for the terms appearing in the granular energy equation as well. Thus, it must be emphasized that while the general forms of the continuity, momentum, and granular energy equations are common among most of the microscopic two-fluid models discussed in the literature, there are variations in the closure relations. Thus, the exact form of the closures for the microscopic two-fluid model is still evolving. Nevertheless, the microscopic two-fluid models are robust in the sense that when they are augmented with physically reasonable closures, they do yield all the known instabilities in gas-particle flows, which in turn lead to persistent fluctuations that take the form of bubble-like voids in dense fluidized beds and clusters and streamers in dilute systems.[3,40,41] Thus, all sets of constitutive relations which capture these small scale instabilities can be expected to lead to similar conclusions regarding the structure of the closures for the filtered equations. With this in mind, we have selected one set of closures for the kinetic theory-based microscopic equations (see Table 1). Further discussion of these equations and an extensive review of the relevant literature can be found in Agrawal et al.[30] As the closures for the microscopic two-fluid models improve, one can easily repeat the analysis described here and refine the filtered closures.

Filtered Two-Fluid Model Equations

The two-fluid model equations are coarse-grained through a filtering operation that amounts to spatial averaging over some chosen filter length scale. In these filtered (a.k.a. coarse-grained) equations, the consequences of the flow structures occurring on a scale smaller than a chosen filter size appear through residual correlations for which one must derive or postulate constitutive models. If constructed properly, and if the several assumptions innate to the filtering methodology hold true, the filtered equations should produce a solution with the same macroscopic features as the finely resolved kinetic theory model solution; however, obtaining this solution should come at less computational cost.

Let $\phi_s(\mathbf{y},t)$ denote the particle volume fraction at location $\mathbf{y}$ and time t obtained by solving the microscopic two-fluid model. We can define a filtered particle volume fraction $\bar{\phi}_s(x,t)$ as

$$\bar{\phi}_s(\mathbf{x},t) = \int_{V_\infty} G(\mathbf{x},\mathbf{y})\phi_s(\mathbf{y},t)d\mathbf{y}$$

where $G(\mathbf{x},\mathbf{y})$ is a weight function that depends on $\mathbf{x}-\mathbf{y}$ and V_∞ denotes the region over which the gas-particle flow occurs. The weight function satisfies $\int_{V_\infty} G(\mathbf{x},\mathbf{y})d\mathbf{y} = 1$. By choosing how rapidly $G(\mathbf{x},\mathbf{y})$ decays with distance measured from $\mathbf{x}$, one can change the filter size. We define the fluctuation in particle volume fraction as

$$\phi_s'(\mathbf{y},t) = \phi_s(\mathbf{y},t) - \bar{\phi}_s(\mathbf{y},t).$$

Filtered phase velocities are defined according to

$$\bar{\phi}_s(\mathbf{x},t)\bar{\mathbf{v}}(\mathbf{x},t) = \int_{V_\infty} G(\mathbf{x},\mathbf{y})\phi_s(\mathbf{y},t)\mathbf{v}(\mathbf{y},t)d\mathbf{y}$$

and

$$(1-\bar{\phi}_s(\mathbf{x},t))\bar{\mathbf{u}}(\mathbf{x},t) = \int_{V_\infty} G(\mathbf{x},\mathbf{y})(1-\phi_s(\mathbf{y},t))\mathbf{u}(\mathbf{y},t)d\mathbf{y}$$

Here, **u** and **v** denote local gas and particle phase velocities appearing in the microscopic two-fluid model. We then define the fluctuating velocities as:

$$\mathbf{v}'(\mathbf{y},t) = \mathrm{v}(\mathbf{y},t) - \bar{\mathrm{v}}(\mathbf{y},t) \quad \text{and} \quad \mathbf{u}'(\mathbf{y},t) = \mathbf{u}(\mathbf{y},t) - \bar{\mathbf{u}}(\mathbf{y},t).$$

Applying such a filter to the continuity Eqs. 1 and 2 in Table 1, we obtain

$$\frac{\partial \rho_s \bar{\phi}_s}{\partial \mathrm{t}} + \nabla\cdot(\rho_s\bar{\phi}_s\bar{\mathbf{v}}) = 0 \tag{13}$$

and

$$\frac{\partial(\rho_g(1-\bar{\phi}_s))}{\partial \mathrm{t}} + \nabla\cdot[(\rho_g(1-\bar{\phi}_s)\bar{\mathbf{u}})] = 0, \tag{14}$$

as the filtered continuity equations, where it has been assumed that the gas density does not vary appreciably over the representative region of the filter. These are identical in form to the microscopic continuity equations in Table 1. Repeating this analysis with the two microscopic momentum balance Eqs. 3 and 4 in Table 1, we obtain the following filtered momentum balances:

$$\left[\frac{\partial(\rho_s\bar{\phi}_s\bar{\mathbf{v}})}{\partial \mathrm{t}} + \nabla\cdot(\rho_s\bar{\phi}_s\bar{\mathbf{v}}\bar{\mathbf{v}})\right] = -\nabla\cdot\Sigma_s - \bar{\phi}\nabla\cdot\bar{\boldsymbol{\sigma}}_g + \bar{\mathbf{F}} + \rho_s\bar{\phi}_s\mathbf{g} \tag{15}$$

$$\left[\frac{\partial(\rho_g(1-\bar{\phi}_s)\bar{\mathbf{u}})}{\partial \mathrm{t}} + \nabla\cdot(\rho_g(1-\bar{\phi}_s)\bar{\mathbf{u}}\bar{\mathbf{u}})\right] = -(1-\bar{\phi}_s)\nabla\cdot\bar{\boldsymbol{\sigma}}_g - \nabla\cdot(\rho_g\overline{(1-\phi_s)\mathbf{u}'\mathbf{u}'}) - \bar{\mathbf{F}} + \rho_g(1-\bar{\phi}_s)\mathbf{g} \tag{16}$$

Here

$$\sum_s = \bar{\sigma}_s + \rho_s\overline{\phi_s\mathbf{v}\mathbf{v}} - \rho_s\bar{\phi}_s\bar{\mathbf{v}}\bar{\mathbf{v}} = \bar{\boldsymbol{\sigma}}_s + \rho_s\overline{\phi_s\mathbf{v}'\mathbf{v}'} \tag{17}$$

$$\bar{\mathbf{F}} = \bar{\mathbf{f}} - \overline{\phi_s'\nabla\cdot\boldsymbol{\sigma}_g'}. \tag{18}$$

The filtered momentum balance equations are nearly identical (in form) to the microscopic momentum balances in Table 1. One exception is that the filtered gas phase momentum balance now contains an additional term, $\nabla\cdot(\rho_g\overline{(1-\phi_s)\mathbf{u}'\mathbf{u}'})$. In the class of problems we consider here the contribution of this term is much weaker than the first and third terms on the right hand side of the gas phase momentum balance equation (as $\rho_s\phi_s \gg \rho_g\ (1-\phi_S)$ in most of the flow domain in the problem considered here).

The effective particle phase stress, Σ_s, includes the filtered microscopic stress $\bar{\boldsymbol{\sigma}}_s$ and a Reynolds stress-like contribution coming from the particle phase velocity fluctuations, see Eq. 17. As noted by Agrawal et al.[30] and Andrews et al.,[31] the contribution due to the velocity fluctuations is much larger than the microscopic particle phase stress even for modestly large filter sizes and this will be seen clearly in the results presented below. Thus, when realistically large filter sizes (of the order of 100 particle diameters or more) are employed, one can neglect the $\bar{\boldsymbol{\sigma}}_s$ contribution for all practical purposes for the particle volume fraction range analyzed in this study. Therefore, at least as a first approximation, it is not necessary to include a filtered granular energy equation in the analysis.[31] This, however, does not imply that the granular energy equation (see Eq. 5 in Table 1) is not important in gas-particle flows. The granular energy equation and the parameters (such as the coefficient of restitution) contained in it will influence the details of the small scale structures, which in turn will affect the velocity fluctuation term in the filtered particle phase stress.

The filtered gas-particle interaction force $\bar{\mathbf{F}}$ includes a filtered gas-particle drag force $\bar{\mathbf{f}}$ and a term representing correlated fluctuations in particle volume fraction and the (microscopic two-fluid model) gas phase stress gradient, see Eq. 18.

Before one can analyze the filtered two-fluid model equations, constitutive relations are needed for the residual correlations $\bar{\mathbf{F}}$, Σ_s, and $\bar{\boldsymbol{\sigma}}_g$ in terms of filtered particle volume fraction, velocities, and pressure. Furthermore, as these are filtered quantities, the constitutive relations capturing them will necessarily depend on the details of the fluctuations being averaged, but these details will depend on the location in the process vessel. For example, one can anticipate that fluctuations in the vicinity of solid boundaries will be different from those away from such boundaries. Accordingly, it is entirely reasonable to expect that the constitutive models for these residual correlations should include some dependence on distance from boundaries. (This is well known in single phase turbulent flows.) In the present study, we do not address the boundary effect, but focus on constitutive models that are applicable in regions away from boundaries as it is an easier first problem to address. It is assumed that the constitutive relations for the residual correlations will depend on local filtered variables and their gradients.

In rapid gas-particle flows with $\rho_s\phi_s \gg \rho_g\ (1-\phi_s)$, it is invariably the case that $\rho_g\overline{(1-\phi_s)\mathbf{u}'\mathbf{u}'} \ll \rho_s\overline{\phi_s\mathbf{v}'\mathbf{v}'}$, and we simplify the filtered gas phase stress as:

$$\bar{\boldsymbol{\sigma}}_g \approx -\overline{p_g}\mathbf{I} \tag{19}$$

We express $\bar{\mathbf{F}}$ as

$$\bar{\mathbf{F}} = \bar{\mathbf{f}} - \overline{\phi_s'\nabla\cdot\boldsymbol{\sigma}_g'} = \bar{\beta}_e(\bar{\mathbf{u}}-\bar{\mathbf{v}}) \tag{20}$$

where $\bar{\beta}_e$ is a filtered drag coefficient to be found. The $\overline{\phi_s'\nabla\cdot\boldsymbol{\sigma}_g'}$ term in Eq. 20 can also add a dynamic part, resembling an apparent added mass force[42–44]; however, as Andrews[45] found such a dynamic part to be much smaller than the drag force term in Eq. 20, we will limit ourselves to Eq. 20.

We begin our analysis by postulating the following filtered particle phase stress model:

$$\sum_s = \overline{p_{se}}\mathbf{I} - \overline{\mu_{be}}(\nabla\cdot\bar{\mathbf{v}})\mathrm{I} - \overline{\mu_{se}}(\nabla\bar{\mathbf{v}} + (\nabla\bar{\mathbf{v}})^{\mathrm{T}} - \frac{2}{3}(\nabla\cdot\bar{\mathbf{v}})\mathbf{I}) \tag{21}$$

where $\overline{p_{se}}(=\overline{p_s}+\frac{1}{3}(\rho_s\overline{\phi_s v'_x v'_x}+\rho_s\overline{\phi_s v'_y v'_y}+\rho_s\overline{\phi_s v'_z v'_z}))$ is the filtered particle phase pressure; $\overline{\mu_{se}}$ and $\overline{\mu_{be}}$ are the filtered particle phase shear and bulk viscosity, respectively. As the simulations described below do not permit an evaluation of $\overline{\mu_{be}}$, we do not consider this term in the present analysis and we simplify Eq. 21 as

$$\sum_s \approx \overline{p_{se}}\mathbf{I}-\overline{\mu_{se}}(\nabla\bar{\mathbf{v}}+(\nabla\bar{\mathbf{v}})^T-\frac{2}{3}(\nabla\cdot\bar{\mathbf{v}})\mathbf{I}). \quad (22)$$

The filtered particle phase shear viscosity is defined as $\overline{\mu_{se}} = \overline{\mu_s} + \rho_s\overline{\phi_s v'_x v'_y}/\overline{\frac{\partial v_x}{\partial y}+\frac{\partial v_y}{\partial x}}$.

We now seek closure relations for $\overline{\beta_e}$, $\overline{p_{se}}$, and $\overline{\mu_{se}}$ by filtering computational data gathered from highly resolved simulations of the microscopic two-fluid model equations.

Detailed Solution of Microscopic Two-Fluid Model Equations

As already noted in the *Filtered Two-fluid Model Equations* section, we restrict our attention to closures for $\overline{\beta_e}$, $\overline{p_{se}}$ and $\overline{\mu_{se}}$ in flow regions far away from solid boundaries. A simple and effective manner by which solid boundaries can be avoided is to consider flows in periodic domains. The filtering operation does not require a periodic domain; however, as each location in a periodic domain is statistically equivalent to any other location, statistical averages can be gathered much faster when simulations are done in periodic domains. With this in mind, all the analyses described here have been performed in periodic domains. Agrawal et al.[30] have already shown that the results obtained from 2D and 3D periodic domains are qualitatively similar, but differ somewhat quantitatively; therefore, we have focused first on 2D simulations in the present study to bring forward the filter size dependence of the closures for the residual correlations, as 2D simulations are computationally less expensive. We will present several 3D simulation results at the end to bring forth the differences between 2D and 3D closures.

Two-Dimensional Simulations

We have performed many sets of highly resolved simulations (of the set of microscopic two-fluid model equations for a fluidized suspension of particles presented in Table 1) in large 2D periodic domains using the open-source software MFIX.[5] These simulations are identical to those described by Agrawal et al.,[30] except that our simulations are now done for much larger domain sizes. Agrawal et al.[30] averaged the residual correlations over the entire domain (i.e., the filter size is the same as their domain size), but as our simulation domains are much larger, the computationally generated "data" can now be averaged using a range of filter sizes that are smaller than the domain size.

After an initial transient period that depends on the initial conditions, persistent, time-dependent and spatially inhomogeneous structures develop. Figure 2 shows an instantaneous snapshot of the particle volume fraction field in one such 2D simulation. One can then select any region of desired size (illustrated in the figure as gray squares of different sizes) and average any quantity of interest over all the cells inside that region; we refer to such results as region-average (or filtered) values. (Such region averaging is equivalent to setting the weight function to an appropriate non-zero constant everywhere inside the region and to zero outside.) Note that one can choose a large number of different regions of the same size inside the overall domain and thus many region-averaged values can be extracted from each instantaneous snapshot. When the system is in a statistical steady state, one can construct tens of thousands of such averages by repeating the analysis at various time instants.

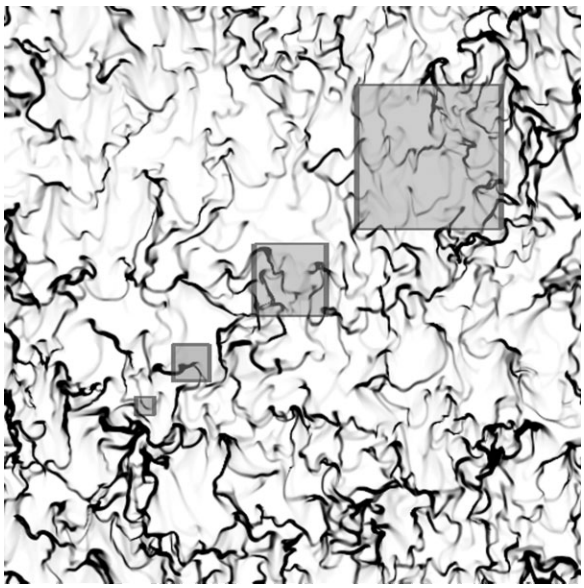

Figure 2. Snapshot of the particle volume fraction field in a large periodic domain of size 131.584 × 131.584 dimensionless units are displayed.

Simulations were performed with 512 × 512 grid points. Overlaid is a pictorial representation of region averaging, where regions of varying size are isolated and treated as individual realizations. Regions (filters) having dimensionless lengths of 4.112, 8.224, 16.448, and 32.896 are shown as shaded subsections.

Returning to Figure 2, note that the averages over different regions at any given time are not equivalent; for example, at the given instant, different regions (even of the same size) will correspond to different region-averaged particle volume fractions, particle and fluid velocities. Thus, one cannot simply lump the results obtained over all the regions; instead, they must be grouped into bins based on various markers and statistical averages must be performed within each bin to extract useful information. Our 2D simulations revealed that the single most important marker for a region is its average particle volume fraction. Therefore, we divided the permissible range of filtered particle volume fraction $(0 \le \bar{\phi}_s < \phi_{s,max} = 0.65)$ into 1300 bins (so that each bin represented a volume fraction window of 0.0005) and classified the filtered data in these bins. (Strictly speaking, one would expect to use two-dimensional bins, involving $\bar{\phi}_s$ and a Reynolds number based on filtered slip velocity, to classify the filtered drag coefficient; however, the Reynolds number dependence was found to be rather weak for the cases investigated in this study.) For each snapshot of the flow field in the statistical

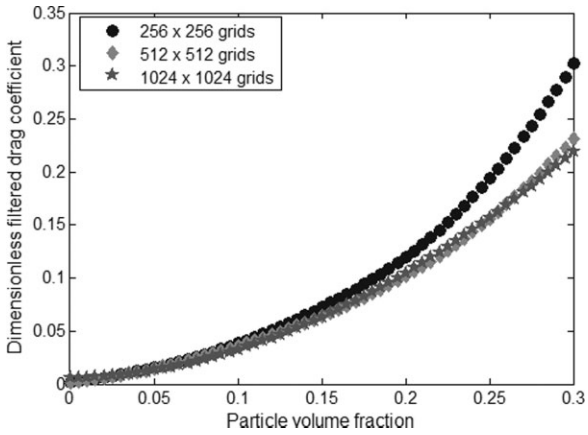

Figure 3. The variation of the dimensionless filtered drag coefficient with particle volume fraction, determined by filtering the computational data gathered from simulations in a large periodic domain of size 131.584 × 131.584 dimensionless units, is presented.

The dimensionless filter length = 8.224. The filtered drag coefficient includes contributions from the drag force and the pressure fluctuation force. Data used for filtering were generated by running simulations for domain-average particle volume fractions of 0.05, 0.15, 0.25, and 0.35. The figure shows results obtained by filtering data generated at different grid resolutions as marked in the legend. The top curve corresponds to result obtained with 256 × 256 grids.

steady state, we considered a filtering region around each grid point in the domain and determined the filtered particle volume fraction $\bar{\phi}_s$, filtered slip velocity $(\bar{\mathbf{u}} - \bar{\mathbf{v}})$, filtered fluid-particle interaction force, and so forth. This combination of filtered quantities represents one realization and it was placed in the appropriate filtered particle volume fraction bin, determined by its volume fraction value. In this manner, a large number of realizations were generated from each snapshot. This procedure was then repeated for many snapshots. The many realizations within each bin were then averaged to determine ensemble-averaged values for each filtered quantity. From such bin statistics, the filtered drag coefficient, the filtered particle phase normal stresses and filtered particle phase viscosity were calculated as functions of filtered particle volume fraction. For example, the filtered drag coefficient is taken to be the ratio of the filtered drag force and the filtered slip velocity, each of which has been determined in terms of the volume fraction. All the results are presented as dimensionless variables, with ρ_s, $\bar{v}$, and g representing characteristic density, velocity, and acceleration.

Figure 3 shows the variation of the dimensionless filtered drag coefficient, $\overline{\beta_{e,d}} = (\overline{\beta_e}\bar{v}_t/\rho_s g)$ as a function of $\bar{\phi}_s$ for one particular filter size. Even though all the results are presented in terms of dimensionless units, it is instructive to consider some dimensional quantities to help visualize the physical problem better. Most of the 2D filtered results presented in this manuscript are based on computational data gathered in a 131.584 × 131.584 (dimensionless units) square periodic domain; this domain size translates to 0.64 m × 0.64 m for the FCC particles (whose physical properties are given in Table 2). The dimensionless filter size of 8.224 used in Figure 3 corresponds to a filter size of 0.04 m for the FCC particles. Thus, one can readily appreciate that this filter size is quite small compared to the macroscopic dimensions of typical process vessels. The various symbols in this figure refer to computational data obtained by solving the microscopic two-fluid model equations at different resolution levels. Simulations were performed using different domain-average particle volume fractions so that every (filtered) volume fraction shown here would have many realizations. This figure indicates that at a sufficiently high resolution the results did become nearly independent of the grid size used in the simulations to generate the computational data. Typically, when the grid size was smaller than the filter size by a factor of 16 or more (so that there were at least 256 grids inside the filtering region in 2D simulations), the filtered results were found to be essentially independent of the grid resolution.

The effect of (periodic) domain size on the filtered drag coefficient was explored by performing simulations with two different domain sizes. Figure 4 presents the dimensionless filtered drag coefficient for two different filter sizes and two different domain sizes. It is clear that for both filter sizes, the results are essentially independent of domain size. In general, the filtered results were found to be independent of the domain size as long as the filter size was smaller than one-fourth of the domain size. (The filter size dependence seen in this figure is discussed below.)

The results presented in Figures 3 and 4, and in many of the figures below, were generated by combining results obtained from simulations with many different specified domain-average particle volume fractions. Figure 5 shows the variation of the filtered drag coefficient with filtered particle volume fraction, with results obtained from simulations with different domain-average particle volume fractions indicated with different symbols. Although the domain-average particle volume fraction affects the filtered drag coefficient slightly

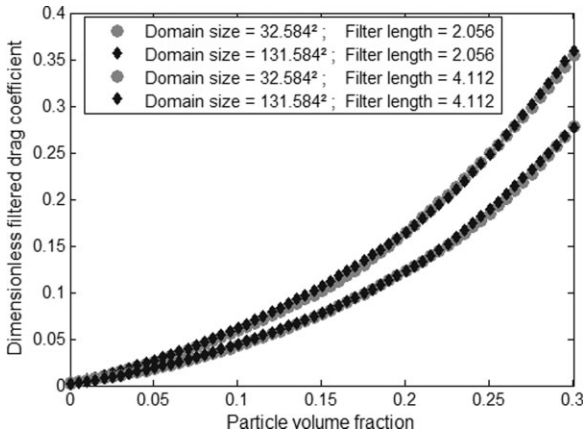

Figure 4. The effect of domain size on the dimensionless filtered drag coefficient is displayed.

Data used for filtering were generated by running simulations at domain-average particle volume fractions of 0.02, 0.05, 0.10, 0.15, 0.20, 0.25, and 0.35 for two different square periodic domains of sizes: 131.584 × 131.584 dimensionless units (512 × 512 grids) and 32.896 × 32.896 dimensionless units (128 × 128 grids). The top two curves correspond to a dimensionless filter length of 2.056, while the bottom two are for a dimensionless filter length of 4.112.

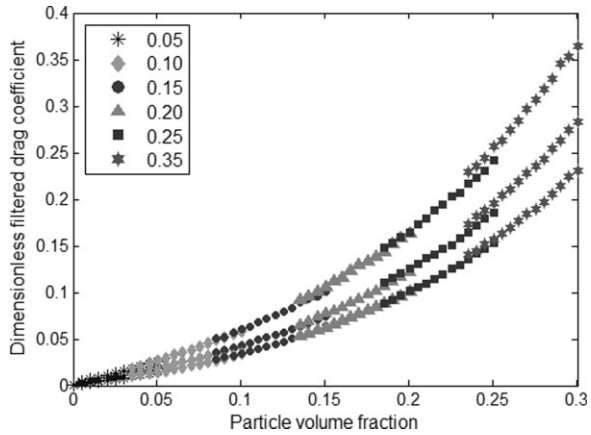

Figure 5. The effect of domain-average particle volume fraction on the dimensionless filtered drag coefficient is displayed.

Simulations were performed in a square domain of size 131.584 × 131.584 dimensionless units and 512 × 512 grid points and domain-average particle volume fractions of 0.05, 0.10, 0.15, 0.20, 0.25, and 0.35 (shown by different symbols in each curve). Results are presented for dimensionless filter lengths of 2.056 (top curve), 4.112 (middle curve) and 8.224 (bottom curve).

(particularly for volume fractions above ~0.20), this effect is clearly much smaller than that of the filter size. Physically, this implies that the filter size dependence manifested in this and other figures largely stems from the inhomogeneous microstructure inside the filtering region and the filtered drag coefficients are either independent of or only weakly dependent on the conditions prevailing outside the filtered region (at least over the range of particle volume fractions over which the data were collected).

Figure 6a shows the variation of the (dimensionless) filtered drag coefficient, as a function of filtered particle volume fraction for various filter sizes. The results for the four smallest filter sizes are likely to decrease somewhat if simulations could be done at higher resolutions, but as noted earlier in the context of Figure 3 the results for all larger filter sizes are essentially independent of grid size. It is clear that the filtered drag coefficient decreases substantially with increasing filter size, and this can readily be rationalized. As the filter size is increased, the averaging is being performed over larger and larger clusters—larger clusters allow greater bypassing of the gas resulting in lower apparent drag coefficient. The uppermost curve in Figure 6a is the intrinsic drag law; the filter size here is simply the grid size used in the simulations of the microscopic two-fluid model equations (which is equivalent to no filtering at all). For typical FCC particles (see Table 2), a dimensionless filter size of 2.056 is equivalent to 0.01 m, and so even at small filter sizes (from an engineering viewpoint) an appreciable reduction occurs in the effective drag coefficient.

Figure 6b shows how the ratio of the filtered drag coefficient to the microscopic drag coefficient changes with particle volume fraction for several filter lengths. It is clear from this figure is that this ratio is only weakly dependent on the particle volume fraction for the range of $0.03 < \phi_s < 0.30$. The ratio within this range can be represented as a function of the filter length only. It can be given in a simple algebraic form as

$$\overline{\beta_e} = \frac{32Fr_f^{-2} + 63.02Fr_f^{-1} + 129}{Fr_f^{-3} + 133.6Fr_f^{-2} + 66.61Fr_f^{-1} + 129}\beta$$

Intuitively, one can expect that the clusters will not grow beyond some critical size and that at sufficiently large filter sizes the filtered drag coefficient will become essentially independent of the filter size. It is clear from Figure 6b that this critical filter size is definitely larger than the largest filter size shown there. Simulations using much larger domains are needed to identify this critical size, but we have not pursued this issue in the present study; instead, we have focused on a qualitative understanding as to how the filtered quantities depend on filter size for modest filter sizes.

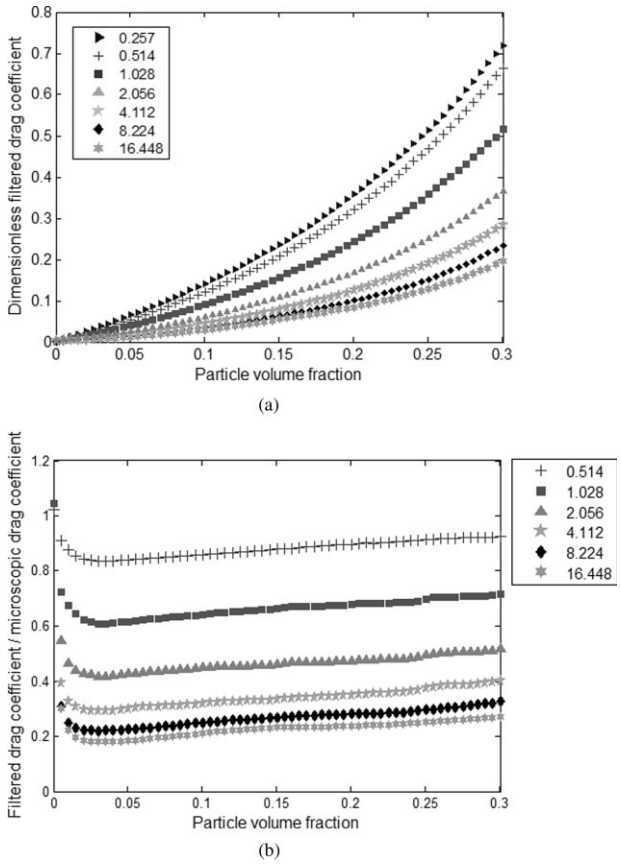

Figure 6. (a) The variation of the dimensionless filtered drag coefficient with particle volume fraction for various filter sizes (listed in the legend in dimensionless units) is shown.

Simulations were performed in a square periodic domain of size 131.584 × 131.584 dimensionless units and using 512 × 512 grid points. Data used for filtering were generated by running simulations for domain-average particle volume fractions of 0.01, 0.02, 0.03, 0.04, 0.05, 0.10, 0.15, 0.20, 0.25, 0.30, and 0.35. The dimensionless filter lengths are shown in the legend. (b) An alternative representation of the filtered drag coefficient. The variation of the dimensionless filtered drag coefficient with particle volume fraction for various filter sizes (listed in the legend in dimensionless units) is shown. All conditions are as in Figure 6a.

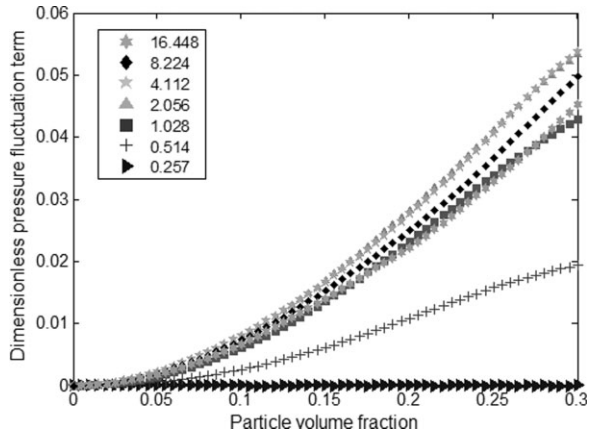

Figure 7. The contribution of the (dimensionless) pressure fluctuation term to the dimensionless filtered drag coefficient shown earlier in Figure 6a is presented.

All conditions are as in Figure 6a. The dimensionless filter lengths are shown in the legend.

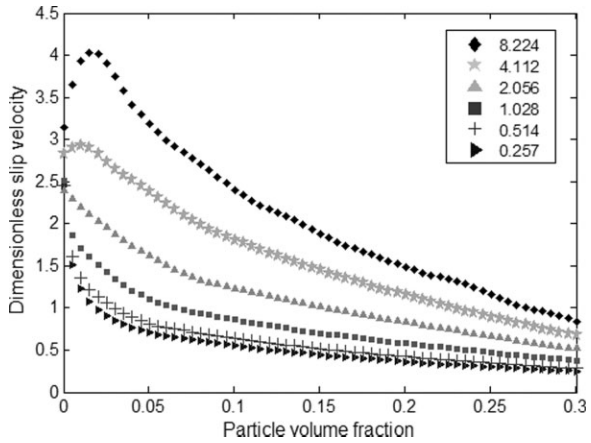

Figure 9. The variation of filtered dimensionless slip velocity with filtered particle volume fraction is shown for various dimensionless filter lengths shown in the legend.

These results were generated from the same set of simulation data that led to Figure 6a.

It was seen earlier, Eq. 18, that the filtered drag force includes contributions from two terms. The second term is essentially equal to $-\phi_s' \nabla p_g'$ as the deviatoric stress in the gas phase is quite small. The contribution from this term to the filtered drag coefficient is presented in Figure 7, while the total contribution due to both terms was shown earlier in Figure 6a. Although the overall filtered drag coefficient decreases with increasing filter size (Figure 6a), the contribution from $-\phi_s' \nabla p_g'$ first increases with the filter size and then decreases (Figure 7). However, $-\phi_s' \nabla p_g'$ contributes no more than 25% of the overall filtered drag coefficient. So, over this range of filter sizes, the primary contribution to $\bar{\mathbf{F}}$ comes from $\bar{\mathbf{f}}$.

The results presented in Figure 6a are plotted in Figure 8 on a logarithmic scale which shows: (a) the typical Richardson–Zaki[46] form for $\bar{\phi}_s$ not too close to zero, and (b) at small $\bar{\phi}_s$ values, a clear departure from this trend. The uppermost curve in this figure corresponds to the intrinsic drag expression extracted simply using a filter size equal to the grid size of the simulations. The two obvious regions manifested by this uppermost curve can be traced to a Reynolds number (Re_g) effect present in the Wen and Yu[6] drag expression used in the simulations. The filtered slip velocity in the vertical direction, as a function of $\bar{\phi}_s$, is shown in Figure 9 for various filter sizes. Here, the bottommost curve is for the case where the filter size is the same as the grid size; the inverse relationship between the local slip velocity and the particle volume fraction is clear. It can be seen from Eq. 7 that β increases with ϕ_s and Re_g; in the uppermost curve in Figure 8, the effect of ϕ_s dominates at high ϕ_s values, while the Re_g effect leads to a reversal of trend at very small ϕ_s values. To establish this point, we carried out simulations where the intrinsic drag coefficient expression (see Eq. 7) was modified by setting $C_D = 24/Re_g$ (so that only the Stokes drag remained). Figure 10 shows the results obtained from these simulations, cf. Figure 8. The uppermost curve in Figure 10 does not show the reversal of trend at very small ϕ_s values, establishing Reynolds number effect as the reason for the difference between the shapes of the uppermost curves in Figures 8 and 10.

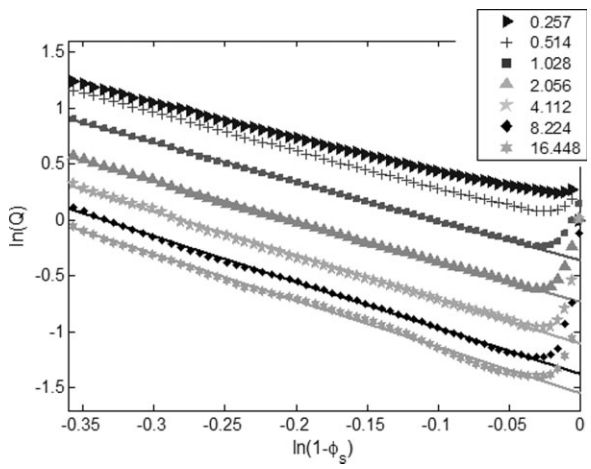

Figure 8. The results shown earlier in Figure 6a are plotted on a natural logarithmic scale.

Here $Q = \frac{\beta_d}{\phi_s \phi_s^g}$, where β_d is the dimensionless filtered drag coefficient, ϕ_s^g is particle volume fraction, and $\phi_g = 1 - \phi_s$ is the gas volume fraction. The dimensionless filter lengths are shown in the legend.

Let us now consider the other curves in both Figures 8 and 10, which are for filter sizes larger than grid size. All of these curves exhibit a Richardson–Zaki like behavior at high volume fractions and a reversal of trend at very low particle volume fractions. This behavior is not due to an Re_g effect in the intrinsic drag law, as Figure 10 does not have any such dependence, and so one has to seek an alternate explanation. The results presented in Figure 9 indicate that one cannot capture this effect through a Reynolds number term involving the filtered slip velocity. Note that for large filter sizes, the slip velocity manifests a peak at some intermediate $\bar{\phi}_s$; for $\bar{\phi}_s$ values to the left of this peak, the filtered slip velocity decreases as $\bar{\phi}_s$ is decreased, while the quantity plotted in Figures 8 and 10 increase with decreasing $\bar{\phi}_s$. Thus, if we seek to capture the data in Figures 8 and 10 in the low $\bar{\phi}_s$ region through a Reynolds number dependence (based on the filtered slip velocity), it will involve a negative

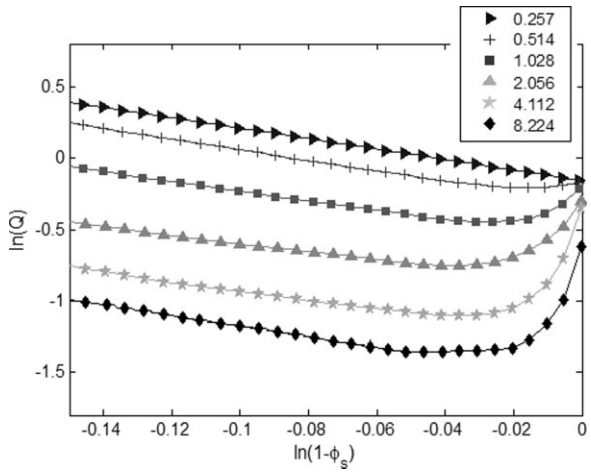

Figure 10. These results are analogous to those shown earlier in Figure 8, with the only difference being that the intrinsic drag force model used in the simulations that led to the present figure did not include a Reynolds number dependence.

The dimensionless filter lengths are shown in the legend.

order dependence, which makes no physical sense. Therefore we attribute the trend reversal seen in Figures 8 and 10 at small $\bar{\phi}_s$ values to just the inhomogeneous microstructure inside the filter region. At low $\bar{\phi}_s$ values, an increase in $\bar{\phi}_s$ increases both the cluster size and particle volume fraction in the clusters; the gas flows around these clusters and the resistance offered by these clusters decreases with increasing cluster size. Large filter sizes average over larger clusters and so the extent of drag reduction observed increases with filter size. At sufficiently large $\bar{\phi}_s$ values, the clusters begin to interact and hindered drag sets in. This behavior is clearly reflected in the vertical slip velocity corresponding to large filter sizes, see Figure 9. The slip velocity increases with $\bar{\phi}_s$ at small $\bar{\phi}_s$ values, consistent with larger and/or denser clusters; it then decreases with increasing $\bar{\phi}_s$ when the clusters begin interact with each other.

It is interesting to note in Figure 9 that the dimensionless slip velocity, in the limit of zero particle volume fraction ($\bar{\phi}_s \to 0$), differs from unity. In our simulations with various domain-average particle volume fractions, regions with $\bar{\phi}_s \to 0$ appeared in the dilute phase surrounding the clusters; here the slip velocity was almost always larger than the terminal velocity. This implies that the gas in the dilute phase was constantly engaged in accelerating the particles upward. This can happen only if the clusters are dynamic in nature with active, continual exchange of particles between the clusters and the dilute phase.

Linear fits of the data in Figure 8 over the particle volume fraction range $(0.075 \le \bar{\phi}_s \le 0.30)$ were used to estimate dimensionless apparent terminal velocity $V_{t,\,app}$ and an apparent Richardson–Zaki exponent, $N_{RZ,app}$.

$$\ln\left(\frac{\bar{\beta}_e v_t}{\rho_s g \bar{\phi}_s(1-\bar{\phi}_s)}\right) = \ln\left(\frac{\overline{\beta_{e,d}}}{\bar{\phi}_s(1-\bar{\phi}_s)}\right) = -(N_{RZ,app}-1)\ln(1-\phi_g) - \ln(V_{t,app}).$$

The variation of $V_{t,app}$ and $N_{RZ,app}$ with dimensionless filter size, $Fr_f^{-1} = g\Delta_f/v_t^2$, are shown in Figures 11a (diamonds), b,

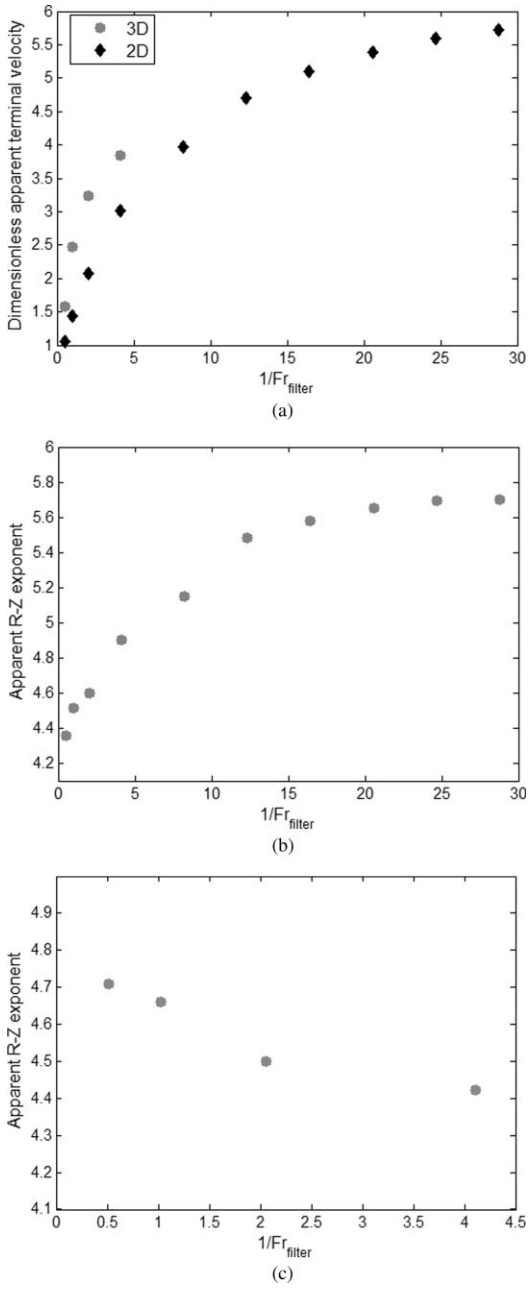

Figure 11. (a) Dimensionless apparent terminal velocity for different dimensionless filter lengths, extracted from results in Figure 8 (2D) for the range $0.075 \le \phi_s \le 0.30$ and those extracted from results in Figure 19 (3D) for the range $0.075 \le \phi_s \le 0.25$.

The solid lines in Figure 8 are based on the apparent terminal velocity shown here and the apparent Richardson–Zaki exponent in Figure 11b. (b) Apparent Richardson–Zaki exponent for different dimensionless filter lengths, extracted from results in Figure 8 (2D) for the range $0.075 \le \phi_s \le 0.30$. The solid line in Figure 8 for a filter length of 2.056 is based on this apparent terminal velocity in Figure 11a and the apparent Richardson–Zaki exponent shown here. (c) Apparent Richardson–Zaki exponent for different dimensionless filter lengths, extracted from results in Figure 19 (3D) for the range $0.075 \le \phi_s \le 0.25$.

respectively. Here, Δ_f denotes the filter size. Both increase with filter size.

Figure 12a shows the variation with $\bar{\phi}_s$ of the dimensionless filtered kinetic theory pressure, $\overline{p_{s,d}} = \overline{p_s}/\rho_s v_t^2$, for the simulations discussed earlier in connection with Figures 4 and 8. At very low $\bar{\phi}_s$ values, the filtered kinetic theory pressure is essentially independent of filter size, but at larger $\bar{\phi}_s$ values distinct filter size dependence becomes clear. Figure 12b shows the dimensionless total particle phase pressure $\overline{p_{se,d}} = \overline{p_{se}}/\rho_s v_t^2$ as a function of $\bar{\phi}_s$ for various filter sizes. Here, the filtered particle phase pressure includes the pressure arising from the streaming and collisional parts captured by the kinetic theory and the subfilter-scale Reynolds-stress like velocity fluctuations (see text below Eq. 21). Comparing Figures 12a, b, it is seen that the contribution resulting from the subfilter-scale velocity fluctuations is much larger than the kinetic theory pressure indicating that, at the coarse-grid scale, one can ignore the kinetic theory contributions to the pressure. It is also clear from Figure 12b that the filtered pressure increases with filter size, a direct consequence of the fact that the energy associated with the velocity fluctuations increases with filter length (as in single phase turbulence). Once again, results obtained from simulations with different domain-average particle volume fractions collapse on to the same curves (as earlier in Figures 5 and 6 for the filtered drag coefficient), confirming that the filtered quantities largely depend on quantities inside the filtering region. The data presented in Figure 12b could be captured by an expression of the form $a\phi_s(1 - b\phi_s)$ with $b \sim 1.80$. The parameter a increases with filter size, see Figure 12c.

Figures 13a, b show the variation with $\bar{\phi}_s$ of dimensionless filtered kinetic theory viscosity, $\overline{\mu_{s,d}} = \overline{\mu_s} g/\rho_s v_t^2$, and the (dimensionless) filtered particle phase shear viscosity, $\overline{\mu_{se,d}} = \overline{\mu_{se}} g/\rho_s v_t^3$. The latter includes the streaming and collisional parts captured by the kinetic theory (shown in Figure 13a) and that associated with the subfilter-scale velocity fluctuations. It is readily seen that for large filter sizes, the contribution from the subfilter scale velocity fluctuations dominate, and the filtered particle phase viscosity increases appreciably with filter size. Once again, results from simulations with different domain-average particle volume fractions collapse on the same curves, adding further support to the viability of the filtering approach. The data presented in Figure 13b could be captured by an expression of the form $c\phi_s(1 - d\phi_s)$ with $d \sim 0.86$. The parameter c increases with filter size; see Figure 13c.

It is mentioned in passing that we have studied the robustness of the filtered statistics against small changes in the secondary model parameters (namely, the coefficient of restitution, density ratio, etc.) and found that they are much less important than the dimensionless filter size; so, capturing the effect of the dimensionless filter size on the dimensionless filtered drag coefficient is indeed the most important challenge.

Agrawal et al.[30] and Andrews et al.[31] determined domain-averaged drag coefficient, particle phase pressure and viscosity by averaging their kinetic theory simulation results over the entire periodic domain. In contrast, we have performed the averaging over regions that are much smaller than the periodic domain, so that the filtered statistics are not affected by the periodic boundary conditions. It is interesting to

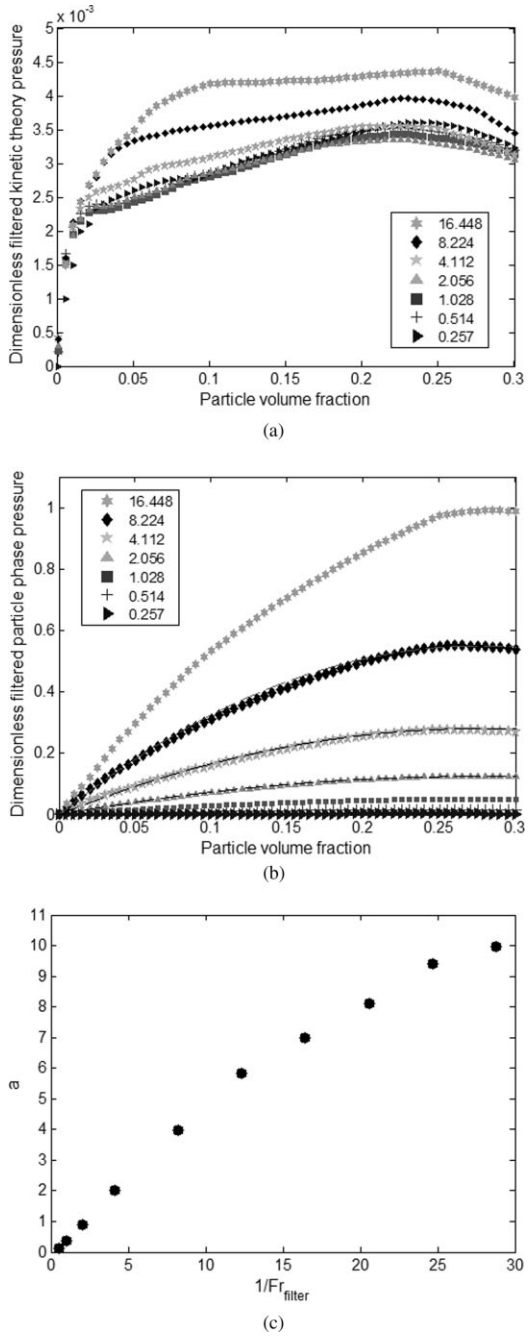

Figure 12. (a) The variation of the dimensionless filtered kinetic theory pressure with particle volume fraction is presented for different dimensionless filter lengths.

The results were extracted from simulations mentioned in the caption for Figure 6a. The dimensionless filter lengths are shown in the legend. (b) The variation of the dimensionless filtered particle phase pressure with particle volume fraction is presented for different dimensionless filter lengths. The results were extracted from simulations mentioned in the caption for Figure 6a. The dimensionless filter lengths are shown in the legend. (c) The coefficient "a" of the dimensionless filtered particle phase pressure in Figure 12b represented as $a\phi_s(1 - b\phi_s)$ (for $\phi_s \leq 0.30$) is plotted against the dimensionless filter length. $b \sim 1.80$ for all filters.

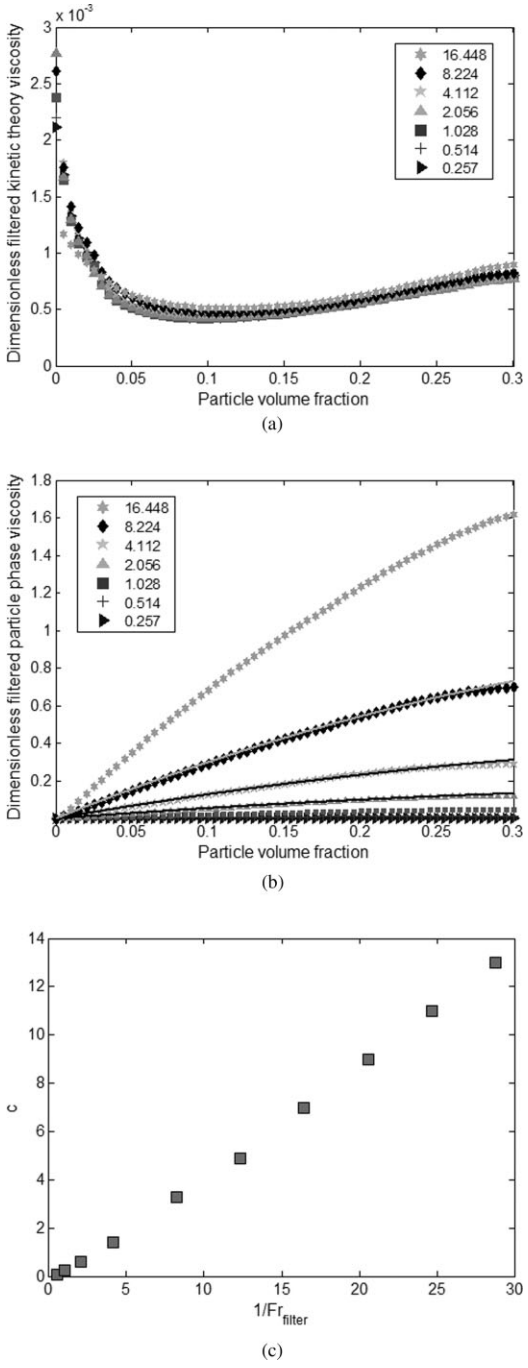

Figure 13. (a) The variation of the dimensionless filtered kinetic theory viscosity with particle volume fraction is presented for different dimensionless filter lengths.

The results were extracted from simulations mentioned in the caption for Figure 6a. The dimensionless filter lengths from the top curve to the bottom curve are shown in the legend. (b) The variation of the dimensionless filtered particle phase viscosity with particle volume fraction is presented for different dimensionless filter lengths. The results were extracted from simulations mentioned in the caption for Figure 6a. The dimensionless filter lengths are shown in the legend. (c) The coefficient "c" of the dimensionless filtered particle phase viscosity in Figure 13b represented as $c\phi_s(1 - d\phi_s)$ (for $\phi_s \leq 0.30$) is plotted against the dimensionless filter length. $d \sim 0.86$ for all filters.

observe that the filter size dependences of all these filtered quantities obtained in our study are qualitatively identical to those reported in the studies of Agrawal et al.[30] and Andrews et al.[31] This further confirms that the robustness of the role played by filter size.

Three-Dimensional Simulations

Figure 14 shows a snapshot of the particle volume fraction field in a 3D periodic domain, and the presence of particle-rich strands is readily visible. Figure 15 shows the effect of grid resolution on the filtered drag coefficient. As seen earlier in Figure 3 for 2D simulations, the dependence of the filtered drag coefficient on grid resolution becomes weaker as the filter size increases. At the lower grid resolution, the filter size of 1.028 is only twice the grid size and when the grid resolution is increased, the filtered drag coefficient changes appreciably. For a filter size of 4.112, there are 512 and 4096 grids inside the filter volume in the two simulations; these are quite large and so the filtered drag coefficient manifests only a weak dependence on resolution.

Figure 16 displays the variation of filtered drag coefficient with particle volume fraction for different filter sizes. As the grid size used in these simulations is 0.257 dimensionless units, the uppermost curve corresponds to using no filter at all. The next curve corresponding to the filter size of 0.514 has only eight grids inside the filtering volume and so is likely to change if simulations with greater resolutions are

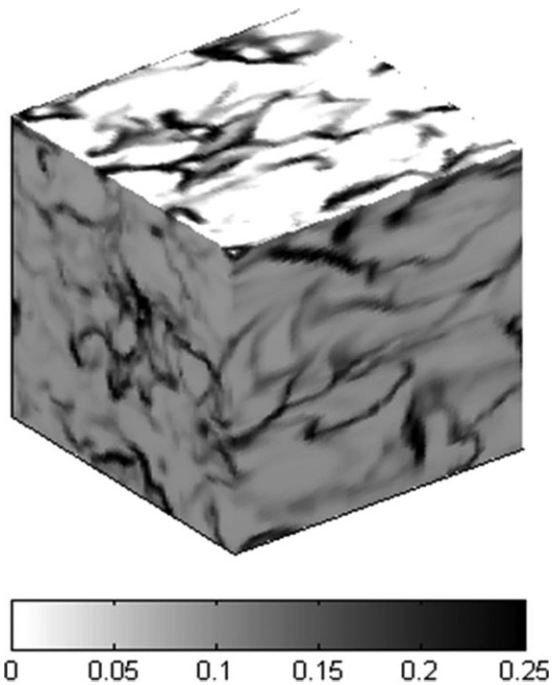

Figure 14. A snapshot of the particle volume fraction field in a large periodic domain of size 16.448 × 16.448 × 16.448 dimensionless units is shown.

Simulation was performed using 64 × 64 × 64 grid points. The domain-average particle volume fraction, $\langle \phi_s \rangle = 0.05$.

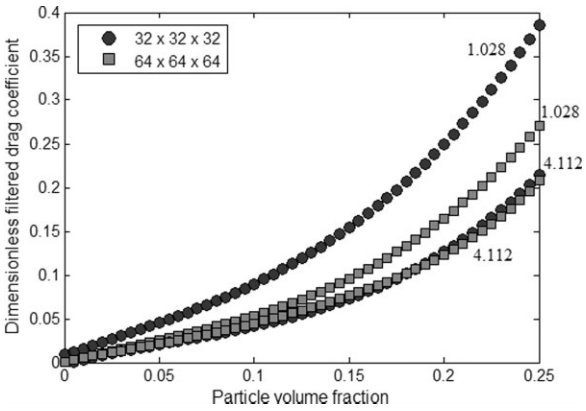

Figure 15. The effect of grid resolution on the dimensionless filtered drag coefficient is presented.

Simulations were performed in a cubic periodic domain of size 16.448 × 16.448 × 16.448 dimensionless units and at two different grid resolutions (32^3 and 64^3). The filtered drag coefficients were calculated for dimensionless filter lengths of 1.028 and 4.112. Data used for filtering were generated by running simulations for domain-average particle volume fractions of 0.05, 0.10, 0.15, 0.20, and 0.35.

performed. The results for filter sizes larger than 2.056 are expected to be nearly independent of grid resolution. It is clear from Figure 16 that the filter size dependence of the filter drag coefficient seen earlier in the 2D simulations persist in 3D as well.

As in the case of 2D simulations, the filtered drag coefficient obtained from 3D simulations at different domain-average particle volume fractions collapse onto the same curve (over the range of volume fractions displayed), see Figure 17. Furthermore, Figure 18 illustrates the filtered drag coefficient is indeed independent of the domain size. These suggest that the

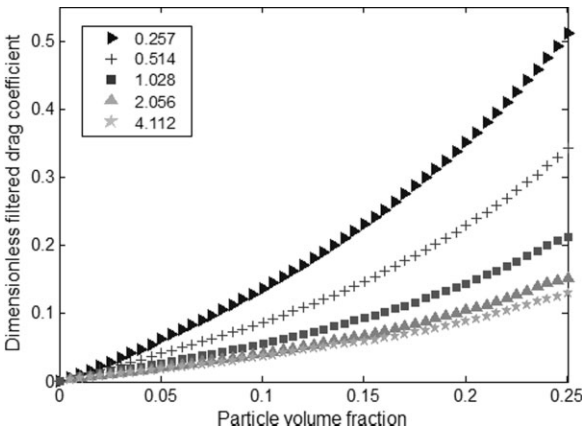

Figure 16. The variation of the dimensionless filtered drag coefficient with particle volume fraction for various filter sizes (listed in the legend in dimensionless units) is shown.

Simulations were in a square domain of size 16.448 × 16.448 × 16.448 dimensionless units, using 64 × 64 × 64 grid points. Data used for filtering were generated by running simulations for domain-average particle volume fractions of 0.01, 0.02, 0.05, 0.10, 0.15, 0.20, 0.25, and 0.35. The dimensionless filter lengths from the top curve to the bottom curve are shown in the legend.

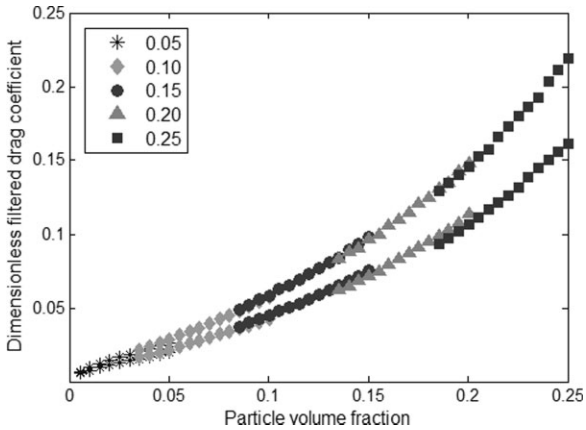

Figure 17. The effect of the domain-average particle volume fraction on the dimensionless filtered drag coefficient is presented.

Simulations were performed in a cubic domain of size 16.448 × 16.448 × 16.448 dimensionless units using 64 × 64 × 64 grid points. The filtered drag coefficients were calculated for dimensionless filter lengths of 1.028 (top curve) and 2.056 (bottom curve). Data used for filtering were generated by running simulations for domain-average particle volume fractions of 0.05, 0.10, 0.15, 0.20, and 0.25 (shown by different symbols in each curve).

filtered drag coefficient is largely determined by the inhomogeneous microstructure inside the filtering volume. The results presented in Figure 16 are plotted on a logarithmic scale in Figure 19. Richardson–Zaki like behavior at high particle volume fractions and a reversal of the trend at lower volume fractions, seen earlier in 2D simulations (see Figure 8), persist in 3D as well. Filter size dependence of the apparent terminal velocity and the exponent in the Richardson–Zaki regime, are shown in Figures 11a, c. The apparent terminal velocity increases with filter size, just as it did for 2D simulations; however, the Richardson–Zaki exponent shows a slight decline with increasing filter size, in marked contrast to 2D simulations

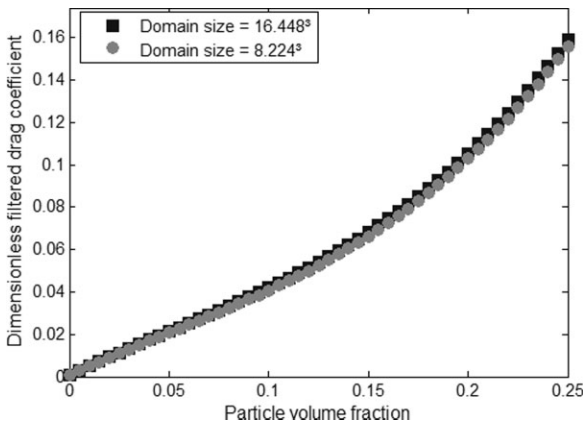

Figure 18. The effect of domain size on the dimensionless filtered drag coefficient is presented for a dimensionless filter length of 2.056.

Simulations were performed at domain-average particle volume fractions of 0.05, 0.15, 0.25, and 0.35 in two different cubic periodic domains of sizes: 16.448 × 16.448 × 16.448 dimensionless units (64 × 64 × 64 grids) and 8.224 × 8.224 × 8.224 dimensionless units (32 × 32 × 32).

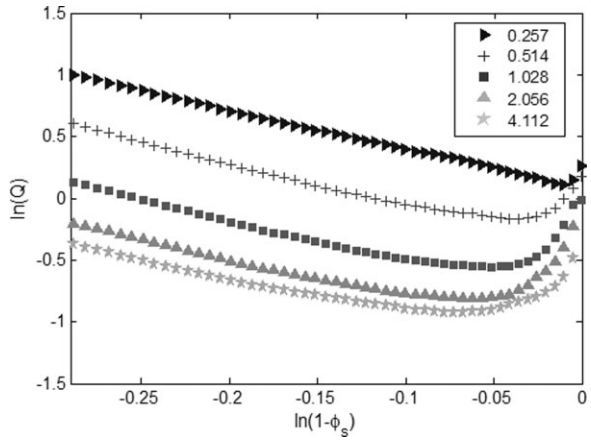

Figure 19. The results shown earlier in Figure 16 are plotted on a natural logarithmic scale.

Here $Q = \frac{\beta_d}{\phi_s \phi_s^g}$, where β_d is the dimensionless filtered drag coefficient, ϕ_s^g is particle volume fraction, and $\phi_g = 1 - \phi_s$ is the gas volume fraction. The dimensionless filter lengths are shown in the legend.

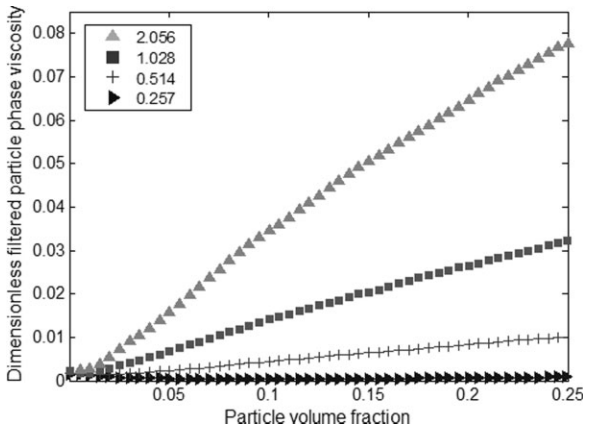

Figure 21. Dimensionless filtered particle phase viscosity for different dimensionless filter lengths, extracted from simulations mentioned in the caption for Figure 16.

The dimensionless filter lengths are shown in the legend.

(see Figure 11b). Thus, there are definite quantitative differences between 2D and 3D results; however, it is clear from Figures 8 and 19 that both 2D and 3D results are strikingly similar.

Figures 20 and 21 present filtered particle phase pressure and viscosity extracted from 3D simulations and can be compared to Figures 12b and 13b, respectively. The strong filter size dependence of these quantities is clearly present in both two- and three-dimensions.

Linear Stability Analysis of the Filtered Two-Fluid Model Equations

If the filtering process and the general form of the filtered constitutive models are meaningful, one would expect that the filtered model equations should afford considerably coarser structures than the microscopic two-fluid models would. We now demonstrate that this is indeed the case.

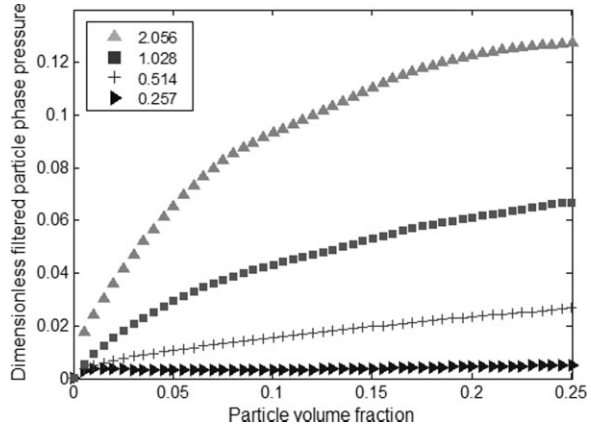

Figure 20. Dimensionless filtered particle phase pressure for different dimensionless filter lengths, extracted from simulations mentioned in the caption for Figure 16.

The dimensionless filter lengths are shown in the legend.

Consider the fate of a small disturbance imposed on a uniformly fluidized bed of infinite extent, as predicted by the filtered model equations. It can readily be shown that the state of uniform fluidization is most unstable to disturbances that take the form of one-dimensional traveling waves having no horizontal structure.[3] The growth rates of such one-dimensional disturbances of various wavenumbers as predicted by the filtered two-fluid model equations, with closures determined in this study for different filter sizes, are presented in Figures 22a, b for uniformly fluidized beds at two different volume fractions. As seen in these figures, the state of uniform fluidization is unstable over a range of wavenumbers (k), $0 < k < k_{HB}$, where k_{HB} denotes the wavenumber at which a Hopf bifurcation occurs.[3] Disturbances whose wavenumber exceed k_{HB} will decay, while those in the range $0 < k < k_{HB}$ will grow Thus, one can expect that the size of the region $0 < k < k_{HB}$ is a measure of the range of wavenumbers that one is most likely to see in transient simulations. It is clear from these figures that k_{HB} decreases monotonically as the filter size is increased, revealing that the larger the filter size the coarser the structures resolved in the filtered two-fluid model are. Thus, the filtering operation has indeed averaged over the fine structures and generated equations and constitutive models that are suitable for integration over coarser grids.

Summary

We have presented a methodology where computational results obtained through highly resolved simulations (in a large periodic domain) of a given microscopic two-fluid model are filtered to deduce closures for the corresponding filtered two-fluid model equations. These filtered closures depend on the filter size and can readily be constructed for a range of filter sizes. To a good approximation, the dimensionless filtered drag coefficient, particle phase pressure and particle phase viscosity can be treated as functions of only

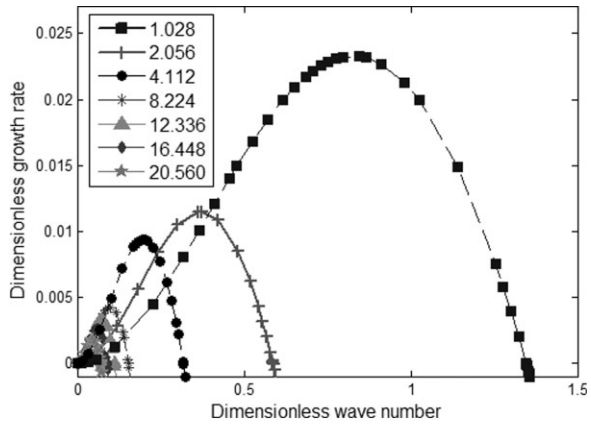

(a)

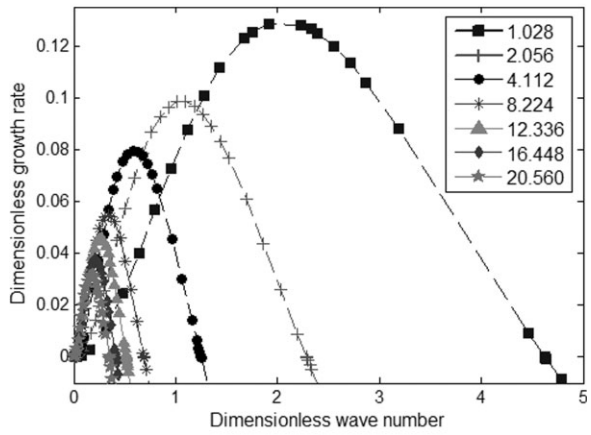

(b)

Figure 22. 1D Linear stability analysis (LSA) of the filtered equations extracted from the 2D simulations for various dimensionless filter lengths shown in the legend. (a) $\langle \phi_s \rangle = 0.15$ (b) $\langle \phi_s \rangle = 0.25$.

particle volume fraction and dimensionless filter size. The effective drag coefficient to describe the interphase interaction force in the filtered equations shows two distinct regimes. At particle volume fractions greater than about 0.075, it follows an effective Richardson–Zaki relationship, and the effective R-Z exponent and apparent terminal velocity have an understandable physical interpretation in terms of interactions between particle clusters instead of the individual particles. At low particle volume fractions, the drag coefficient shows an anomalous behavior that is consistent with the formation of larger and denser clusters with increasing particle volume fraction.

The velocity fluctuations associated with the very complicated inhomogeneous structures shown by the microscopic two-fluid simulations dictate the magnitudes of the filtered particle phase pressure, and viscosity. The contributions of the kinetic theory pressure and viscosity to these filtered quantities are negligibly small and so, for practically relevant filter sizes, one need not include the filtered granular energy equation in the analysis. This, however, does not mean that the fluctuations at the level of the individual particles, which the kinetic theory strives to model, are not important; these fluctuations influence the inhomogeneous microstructure and their velocity fluctuations, and hence the closures for the filtered equations.

Linear stability analysis of the filtered two-fluid model equations, with closures corresponding to several different filter lengths, showed that filtering is indeed erasing the fine structure and only presenting coarser structures.

It is clear from our simulation results that there is a striking similarity between the 2D and 3D results. Although there are quantitative differences between 2D and 3D, the following characteristics were found to be common between them:

(a) The filtered drag coefficient decreased with increasing filter size, and (b) The filtered particle phase pressure and viscosity increased with filter size. It seems reasonable to expect that the clusters will not grow beyond some critical size; if this is indeed the case, the filtered drag coefficient, and particle phase pressure and viscosity will become nearly independent of the filter size beyond some critical value. It is important to understand if such saturation occurs and, if so, at what filter size. It is also important to incorporate the effects of bounding walls on the filtered closures as comparison of the filtered model predictions with experimental data cannot be pursued until this issue is addressed. These are fertile problems for further research.

In the present study, the $-\overline{\phi_s' \nabla p_g'}$ term has been absorbed into the filtered the drag force. Zhang and VanderHeyden[42] and de Wilde[43,44] argue that $-\overline{\phi_s' \nabla p_g'}$ should also include a dynamic part (namely, an added mass force). Andrews[45] found in his simulation study that the principal contribution of $-\overline{\phi_s' \nabla p_g'}$ was to a filtered drag force term, which has been included in our study. A more thorough investigation of the dynamic contribution would also be of interest.

Acknowledgments

This work was supported by the US Department of Energy (grants: CDE-FC26-00NT40971 and DE-PS26-05NT42472-11) and the ExxonMobil Research and Engineering Company. Andrews and Igci acknowledge summer training on MFIX at the National Energy Technology Laboratory, Morgantown, WV. The authors thank Madhava Syamlal, Chris Guenther, Ronald Breault, and Sofiane Benyahia for their assistance throughout the course of this study.

Notation

C_D = single particle drag coefficient
d = particle diameter, m
e_p = coefficient of restitution for particle–particle collisions
$\mathbf{f}$ = interphase interaction force per unit volume in the microscopic two-fluid model, kg/m^2 s^2
$\bar{\mathbf{f}}$ = filtered value of $\mathbf{f}$, kg/m^2 s^2
$\bar{\mathbf{F}}$ = interphase interaction force per unit volume in the filtered two-fluid model, kg/m^2 s^2
Fr_f = Froude number based on filter size = $v_t^2/g\Delta_f$
g, $\mathbf{g}$ = acceleration due to gravity, m/s^2
g_O = value of radial distribution function at contact (see expression in Table 1)
$G(\mathbf{x},\mathbf{y})$ = weight function, m^{-3}
J_{coll} = rate of dissipation of granular energy per unit volume by collisions between particles, kg/m s^3
J_{vis} = rate of dissipation of granular energy per unit volume by the relative motion between gas and particles, kg/m s^3
$N_{RZ,app}$ = apparent Richardson–Zaki exponent

p_g, p_s = gas and particle phase pressures in the microscopic two-fluid model, respectively, kg/m s^2
$\overline{p_g}$, $\overline{p_s}$ = filtered value of p_g and p_s, respectively, kg/m s^2
$\overline{p_{s,d}} = \overline{p_s}$ made dimensionless; $\overline{p_{s,d}} = \overline{p_s}/\rho_s v_t^2$
$\overline{p_{se}}$ = filtered particle phase pressure, kg/m s^2
$\overline{p_{se,d}} = \overline{p_{se}}$ made dimensionless; $\overline{p_{se,d}} = \overline{p_{se}}/\rho_s v_t^2$
$\mathbf{q}$ = flux of granular energy, kg/s^3
Re_g = single particle Reynolds number
t = time, s
T = granular temperature, m^2/s^2
$\mathbf{u}$, $\mathbf{v}$ = gas and particle phase velocities in the microscopic two-fluid model, respectively, m/s
$\bar{\mathbf{u}}$, $\bar{\mathbf{v}}$ = filtered gas and particle phase velocities, respectively, m/s
$\mathbf{u}'$, $\mathbf{v}'$ = fluctuations in gas and particle phase velocities, respectively, m/s
v_t = terminal settling velocity, m/s
$V_{t,app}$ = dimensionless apparent terminal velocity
$\mathbf{x}$, $\mathbf{y}$ = position vectors, m

Greek letters

β = drag coefficient in the microscopic two-fluid model, kg/m^3 s
$\overline{\beta_e}$ = filtered drag coefficient, kg/m^3 s
$\overline{\beta_{e,d}}$ = dimensionless filtered drag coefficient = $\overline{\beta_e} v_t/\rho_s g$
ϕ_s, ϕ_g = particle and gas phase volume fractions, respectively
$\bar{\phi}_s, \bar{\phi}_g$ = filtered particle and gas phase volume fractions, respectively
ϕ_s' = fluctuation in particle phase volume fraction
$\langle \phi_s \rangle$ = domain-average particle volume fraction
$\phi_{s,max}$ = maximum particle volume fraction
ρ_s, ρ_g = particle and gas densities, respectively, kg/m^3
Δ_f = filter size, m
σ_s, σ_g = particle and gas phase stress tensors in the microscopic two-fluid model, respectively, kg/m s^2
$\bar{\sigma}_s, \bar{\sigma}_g$ = filtered values of σ_s and σ_g, respectively, kg/m s^2
Σ_s = filtered total particle phase stress, kg/m s^2
Γ_{slip} = rate of generation of granular energy per unit volume by gas-particle slip, kg/m s^3
$\eta, \alpha, \lambda, \mu$ = quantities defined in Table 1
λ^*, μ^* = quantities defined in Table 1
λ_s = granular thermal conductivity, kg/m s
μ_g = gas phase viscosity, kg/m s
$\hat{\mu}_g$ = effective gas phase viscosity appearing in the microscopic two-fluid model (taken to be equal to μ_g itself in our simulations) kg/m s
μ_b, μ_g = bulk and shear viscosities of the particle phase appearing in the kinetic theory model, kg/m s
$\overline{\mu_{s,d}} = \mu_s$ made dimensionless; $\overline{\mu_{s,d}} = \overline{\mu_s} g/\rho_s v_t^3$
$\overline{\mu_{be}}, \overline{\mu_{se}}$ = bulk and shear viscosities of the particle phase appearing in the filtered two-fluid model, kg/m s
$\overline{\mu_{se,d}} = \overline{\mu_{se}}$ made dimensionless; $\overline{\mu_{se,d}} = \overline{\mu_{se}} g/\rho_s v_t^3$

Literature Cited

1. Grace JR, Bi H. In: Grace JR, Avidan AA, Knowlton TM, editors. *Circulating Fluidized Beds*, 1st ed. New York: Blackie Academic & Professional, 1997; Chapter 1; pp 1–20.
2. Gidaspow D. *Multiphase Flow and Fluidization*. CA: Academic Press, 1994; Chapter 4; pp 99–152.
3. Jackson R. *The Dynamics of Fluidized Particles*. Cambridge University Press, 2000.
4. Syamlal M, Rogers W, O'Brien TJ. *MFIX Documentation*. Morgantown, WV: U.S. Department of Energy, Federal Energy Technology Center, 1993.
5. Syamlal M. *MFIX Documentation: Numerical Techniques*. DOE/MC-31346-5824. NTIS/DE98002029; 1998. Also see www.mfix.org.
6. Wen CY, Yu YH. Mechanics of fluidization. *Chem Eng Prog Symp Ser*. 1966;62:100–111.
7. Ergun S. Fluid flow through packed columns. *Chem Eng Prog*. 1952;48:89–94.
8. Hill RJ, Koch DL, Ladd AJC. The first effects of fluid inertia on flow in ordered and random arrays of spheres. *J Fluid Mech*. 2001; 448:213–241.
9. Hill RJ, Koch DL, Ladd AJC. Moderate-Reynolds-number flows in ordered and random arrays of spheres. *J Fluid Mech*. 2001;448:243–278.
10. Wylie JJ, Koch DL, Ladd AJC. Rheology of suspensions with high particle inertia and moderate fluid inertia. *J Fluid Mech*. 2003; 480: 95–118.
11. Khandai D, Derksen JJ, van den Akker HEA. Interphase drag coefficients in gas-solid flows. *AIChE J*. 2003;49:1060–1063.
12. Li J, Kuipers JAM. Gas-particle interactions in dense gas-fluidized beds. *Chem Eng Sci*. 2003;58:711–718.
13. van der Hoef MA, Boetstra R, Kuipers JAM. Lattice Boltzmann simulations of low Reynolds number flow past mono- and bi-disperse arrays of spheres: results for the permeability and drag forces. *J Fluid Mech*. 2005;528:233–254.
14. Benyahia S, Syamlal M, O'Brien TJ. Extension of Hill-Koch-Ladd drag correlation over all ranges of Reynolds number and solids volume fraction. *Powder Technol*. 2006;162:166–174.
15. Gidaspow D, Jung J, Singh RJ. Hydrodynamics of fluidization using kinetic theory: an emerging paradigm. 2002 Fluor-Daniel Lecture. *Powder Technol*. 2004;148:123–141.
16. Koch DL, Sangani AS. Particle pressure and marginal stability limits for a homogeneous monodisperse gas fluidized bed: kinetic theory and numerical simulations. *J Fluid Mech*. 1999;400:229–263.
17. Huilin L, Yurong H, Gidaspow D, Lidan Y. Yukun Q. Size segregation of binary mixture of solids in bubbling fluidized beds. *Powder Technol*. 2003;134:86–97.
18. Iddir H, Arastoopour H, Hrenya CM. Analysis of binary and ternary granular mixtures behavior using the kinetic theory approach. *Powder Technol*. 2005;151:117–125.
19. Arnarson BO, Jenkins JT. Binary mixtures of inelastic spheres: simplified constitutive theory. *Phys Fluids*. 2004;16:4543–4550.
20. Jenkins J, Mancini F. Kinetic theory for binary mixtures of smooth, nearly elastic spheres. *Phys Fluids A*. 1989;1:2050–2057.
21. Benyahia S, Arastoopour H, Knowlton TM. Simulation of particles and gas flow behavior in the riser section of a circulating fluidized bed using the kinetic theory approach for the particulate phase. *Powder Technol*. 2000;112:24–33.
22. Ding J, Gidaspow D. A Bubbling fluidization model using kinetic-theory of granular flow. *AIChE J*. 1990;36:523–538.
23. Goldschmidt MJV, Kuipers JAM. van Swaaij WPM. Hydrodynamic modeling of dense gas-fluidized beds using the kinetic theory of granular flow: effect of restitution coefficient on bed dynamics. *Chem Eng Sci*. 2001;56:571–578.
24. Neri A, Gidaspow D. Riser hydrodynamics: simulation using kinetic theory. *AIChE J*. 2000;46:52–67.
25. Lun CKK, Savage SB, Jeffrey DJ, Chepurniy N. Kinetic theories of granular flows: inelastic particles in Couette flow and slightly inelastic particles in a general flow field. *J Fluid Mech*. 1984;140:223–256.
26. Sinclair JL, Jackson R. Gas-particle flow in a vertical pipe with particle-particle interaction. *AIChE J*. 1989;35:1473–1486.
27. Pita JA, Sundaresan S. Gas-solid flow in vertical tubes. *AIChE J*. 1991;37:1009–1018.
28. Pita JA, Sundaresan S. Developing flow of a gas-particle mixture in a vertical riser. *AIChE J*. 1993;39:541–552.
29. Louge M, Mastorakos E, Jenkins JT. The role of particle collisions in pneumatic transport. *J Fluid Mech*. 1991;231:345–359.
30. Agrawal K, Loezos PN, Syamlal M, Sundaresan S. The role of meso-scale structures in rapid gas-solid flows. *J Fluid Mech*. 2001; 445:151–185.
31. Andrews AT IV, Loezos PN, Sundaresan S. Coarse-grid simulation of gas-particle flows in vertical risers. *Ind Eng Chem Res*. 2005;44: 6022–6037.
32. Sundaresan S. Perspective: modeling the hydrodynamics of multiphase flow reactors: current status and challenges. *AIChE J*. 2000; 46:1102–1105.
33. O'Brien TJ, Syamlal M. Particle cluster effects in the numerical simulation of a circulating fluidized bed. In: Avidan A, editor. *Circulating Fluidized Bed Technology. IV. Proceedings of the Fourth International Conference on Circulating Fluidized Beds*, Hidden Valley Conference Center and Mountain Resort, Somerset, PA, August 1–5, 1993.

34. Boemer A, Qi H, Hannes J, Renz U. Modelling of solids circulation in a fluidised bed with Eulerian approach. 29th IEA-FBC Meeting in Paris, France, Nov. 24–26, 1994.
35. Heynderickx GJ, Das AK, de Wilde J, Marin GB. Effect of clustering on gas-solid drag in dilute two-phase flow. *Ind Eng Chem Res*. 2004;43:4635–4646.
36. McKeen T, Pugsley T. Simulation and experimental validation of a freely bubbling bed of FCC catalyst. *Powder Technol*. 2003;129: 139–152.
37. Yang N, Wang W, Ge W, Wang L. Li, J. Simulation of heterogeneous structure in a circulating fluidized bed riser by combining the two-fluid model with EMMS approach. *Ind Eng Chem Res*. 2004; 43:5548–5561.
38. Dasgupta S, Jackson R, Sundaresan S. Turbulent gas-particle flow in vertical risers. *AIChE J*. 1994;40:215–228.
39. Hrenya CM, Sinclair JL. Effects of particle-phase turbulence in gas-solid flows. *AIChE J*. 1997;43:853–869.
40. Glasser BJ, Sundaresan S, Kevrekidis IG. From bubbles to clusters in fluidized beds. *Phys Rev Lett*. 1998;81:1849–1852.
41. Glasser BJ, Kevrekidis IG, Sundaresan S. One- and two-dimensional travelling wave solutions in gas-fluidized beds. *J Fluid Mech*. 1996; 306:183–221.
42. Zhang DZ, VanderHeyden WB. The effects of mesoscale structures on the macroscopic momentum equations for two-phase flows. *Int J Multiphase Flow*. 2002;28:805–822.
43. De Wilde J. Reformulating and quantifying the generalized added mass in filtered gas-solid flow models. *Phys Fluids*. 2005;17:1–14.
44. De Wilde J. The generalized added mass revised. *Phys Fluids*. 2007;19:1–4.
45. Andrews AT IV. Filtered models for gas-particle hydrodynamics. PhD Dissertation, Princeton University, Princeton, NJ, 2007.
46. Richardson JF, Zaki WN. Sedimentation and fluidization. I. *Trans Inst Chem Eng*. 1954;32:35–53.

Manuscript received Sept. 26, 2007, and revision received Feb. 14, 2008.